Nuclear Inst. and Methods in Physics Research, A 867 (2017) 115–127

Contents lists available at ScienceDirect

Nuclear Inst. and Methods in Physics Research, A

journal homepage: www.elsevier.com/locate/nima

Design and construction of a high-energy photon polarimeter

M. Dugger [a,*], B.G. Ritchie [a], N. Sparks [a], K. Moriya [a], R.J. Tucker [a], R.J. Lee [a], B.N. Thorpe [a], T. Hodges [a], F.J. Barbosa [b], N. Sandoval [b], R.T. Jones [c]

[a] Arizona State University, Tempe, AZ 85287-1504, United States
[b] Thomas Jefferson National Accelerator Facility, Newport News, VA 23606, United States
[c] University of Connecticut, Storrs, CT 06269, United States

ARTICLE INFO

Keywords:
Polarized photon beam
Beam characteristics
Polarization measurement
Triplet photoproduction

ABSTRACT

We report on the design and construction of a high-energy photon polarimeter for measuring the degree of polarization of a linearly-polarized photon beam. The photon polarimeter uses the process of pair production on an atomic electron (triplet production). The azimuthal distribution of scattered atomic electrons following triplet production yields information regarding the degree of linear polarization of the incident photon beam. The polarimeter, operated in conjunction with a pair spectrometer, uses a silicon strip detector to measure the recoil electron distribution resulting from triplet photoproduction in a beryllium target foil. The analyzing power Σ_A for the device using a 75 μm beryllium converter foil is about 0.2, with a relative systematic uncertainty in Σ_A of 1.5%.

1. Introduction

Multi-GeV polarized photon beams provide a precision tool for probing excitations of the quark and gluon substructures of mesons and baryons. A common approach for producing multi-GeV linearly-polarized photon beams is the coherent bremsstrahlung process, in which a high-energy electron beam undergoes bremsstrahlung within an oriented diamond crystal. Enhancements in the resulting photon spectrum possess linear polarization. The degree and direction of linear polarization are controlled by the relative orientation of the diamond symmetry axes with respect to the incident electron beam.

We report here the development of a photon beam polarimeter based on measuring the polarization of a multi-GeV photon beam using the so-called "triplet photoproduction" process [1,2]. Such a "triplet polarimeter" determines the degree of polarization of the incident photon beam by using the process of triplet photoproduction. In the triplet photoproduction process, the polarized photon beam interacts with the electric field of an atomic electron (rather than the field of the atomic nucleus) within the material of a production target, and produces a high energy electron–positron pair through the pair production process. The atomic electron on which the pair production took place then recoils with sufficient momentum to leave the atom and, if the recoil momentum is large enough and the production target thin enough, the electron can leave the target material altogether. Any momentum of the electron–positron pair transverse to the incoming photon beam must be compensated by the momentum of the recoil electron. Typically the momentum of the recoil electron is much smaller than that of either of the pair-produced leptons, so the recoil electron can attain a large polar scattering angle relative to the axis determined by the incoming photon beam. When coupled with the trajectory and energy information of the lepton pair, the azimuthal angular distribution of the recoil electron can provide a measure of the photon beam polarization.

This report is organized in the following fashion. We initially provide a description of the triplet photoproduction process in terms of quantum electrodynamics (QED), and show that such a description accurately represents the experimentally observed cross section for the process. Next, the design of the triplet polarimeter (TPOL) in use within Hall D of the Thomas Jefferson National Accelerator Facility (Jefferson Lab) is discussed in order to indicate how considerations of the features of Hall D are reflected in the design of the device, followed by a discussion of details of the construction of the TPOL. We then describe the analysis of Spring 2016 data, and systematic uncertainties in the photon-beam polarization estimate.

2. The triplet photoproduction process

The cross section for triplet photoproduction can be written as $\sigma_t = \sigma_0 [1 - P\Sigma\cos(2\phi)]$ for a polarized photon beam, where σ_0 is the unpolarized cross section, P the photon beam polarization, Σ the beam

---

[*] Corresponding author.

http://dx.doi.org/10.1016/j.nima.2017.05.026
Received 23 March 2017; Received in revised form 17 May 2017; Accepted 18 May 2017
Available online 12 June 2017

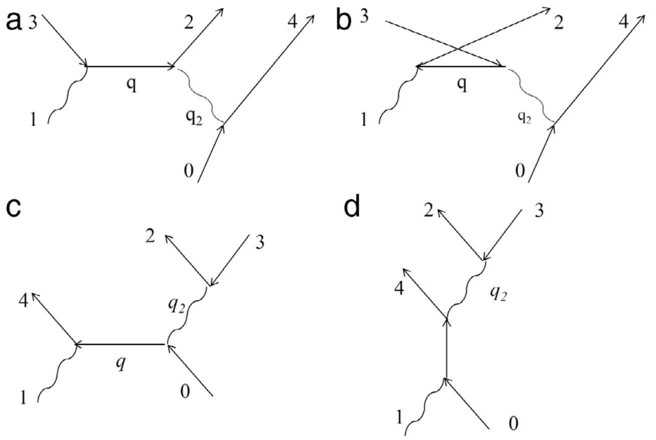

Fig. 1. The diagrams involved in a QED calculation of the triplet photoproduction process. This figure illustrates one-half of the Feynman diagrams involved in the triplet photoproduction process; the remaining half is obtained by exchanging the electron at 2 with the electron at 4. Diagrams (a) and (b) are referred to as "$\gamma\gamma$-like", while diagrams (c) and (d) are said to be "Compton-like". For the figures, line 0 represents the target electron, line 1 is the incident photon, lines 2 and 3 are the pair-produced electron and positron, respectively, and line 4 is the recoil atomic electron.

asymmetry for the process, and ϕ the azimuthal angle of the trajectory of the recoil electron with respect to the plane of polarization for the incident photon beam. To determine the photon beam polarization, the azimuthal distribution of the recoil electrons is recorded and fit to the function $A\,[1 - B\cos(2\phi)]$, where the variables A and B are parameters of the fit. In principle, once B has been extracted from the data, the degree of photon beam polarization is given by $P = B/\Sigma$. The triplet photoproduction process is governed solely by QED, so the beam asymmetry Σ can be directly calculated to leading order in α_{QED}. We now turn to a description of how such a calculation has been performed for this report.

2.1. QED diagrams in the triplet photoproduction process

A QED calculation of the triplet photoproduction process includes all 8 tree-level QED diagrams shown in Fig. 1, with corrections due coherent scattering (also referred to as the screening correction) included. We now discuss the various terms in Fig. 1 in turn, indicating the contribution of each to the full calculation.

2.1.1. $\gamma\gamma$-like diagrams

Diagrams (a) and (b) in Fig. 1 are referred to here as "$\gamma\gamma$-like". These diagrams resemble the reaction $\gamma\gamma \to e^+e^-$, where one of the γ legs is connected to an electron at position 0 that scatters to position 4.

The matrix elements for the $\gamma\gamma$-like diagrams are

$$\begin{aligned} -\,iM_a \equiv{}& (ig_e)^3\left(\frac{-i}{q_2^2}\right) \\ &\times\left[\bar{u}_2\gamma^\mu i\left(\frac{\not{p}_1-\not{p}_3+m}{(p_1-p_3)^2-m^2}\right)\not{\epsilon}_1 v_3\right]\left[\bar{u}_4\gamma_\mu u_0\right], \end{aligned} \tag{1}$$

$$\begin{aligned} -\,iM_b \equiv{}& (ig_e)^3\left(\frac{-i}{q_2^2}\right) \\ &\times\left[\bar{u}_2\not{\epsilon}_1 i\left(\frac{\not{p}_2-\not{p}_1+m}{(p_2-p_1)^2-m^2}\right)\gamma^\mu v_3\right]\left[\bar{u}_4\gamma_\mu u_0\right], \end{aligned} \tag{2}$$

where γ_μ represents the Dirac matrices, m the electron mass, q_2^2 the mass of the virtual photon, p ($\not{p}$) the four-momentum (product of four-momentum with the Dirac matrices), u and v represent spinors, $\bar{u}$ is an adjoint spinor, $\not{\epsilon}_1$ is the product of incident photon polarization and Dirac matrices, and the coupling constant g_e is equal to $\sqrt{4\pi\alpha}$, with α being the fine structure constant. The subscripts 0, 1, 2, 3, and 4 represent the target electron, incident photon, outgoing electron, outgoing positron, and recoil electron, respectively.

The matrix elements for the crossed $\gamma\gamma$-like diagrams (which are not shown in Fig. 1) are found by switching legs 2 and 4 of diagrams (a) and (b) in Fig. 1. Those matrix elements are written as

$$\begin{aligned} -\,iM_{a2} \equiv{}& (ig_e)^3\left(\frac{i}{q_2^2}\right) \\ &\times\left[\bar{u}_4\gamma^\mu i\left(\frac{\not{p}_1-\not{p}_3+m}{(p_1-p_3)^2-m^2}\right)\not{\epsilon}_1 v_3\right]\left[\bar{u}_2\gamma_\mu u_0\right], \end{aligned} \tag{3}$$

$$\begin{aligned} -\,iM_{b2} \equiv{}& (ig_e)^3\left(\frac{i}{q_2^2}\right) \\ &\times\left[\bar{u}_4\not{\epsilon}_1 i\left(\frac{\not{p}_4-\not{p}_1+m}{(p_4-p_1)^2-m^2}\right)\gamma^\mu v_3\right]\left[\bar{u}_2\gamma_\mu u_0\right]. \end{aligned} \tag{4}$$

2.1.2. Compton-like diagrams

Diagrams (c) and (d) in Fig. 1 are referred to here as "Compton-like". These two diagrams resemble the reaction $\gamma e \to \gamma e$, where the scattered γ leg is connected to an electron–positron creation vertex.

The matrix elements for Compton-like diagrams are

$$\begin{aligned} -\,iM_c \equiv{}& (ig_e)^3\left(\frac{-i}{q_2^2}\right) \\ &\times\left[\bar{u}_4\not{\epsilon}_1 i\frac{\not{p}_4-\not{p}_1+m}{(p_4-p_1)^2-m^2}\gamma^\mu u_0\right]\left[\bar{u}_2\gamma_\mu v_3\right], \end{aligned} \tag{5}$$

$$\begin{aligned} -\,iM_d \equiv{}& (ig_e)^3\left(\frac{-i}{q_2^2}\right) \\ &\times\left[\bar{u}_4\gamma^\mu i\frac{\not{p}_1+\not{p}_0+m}{(p_1+p_0)^2-m^2}\not{\epsilon}_1 u_0\right]\left[\bar{u}_2\gamma_\mu v_3\right]. \end{aligned} \tag{6}$$

Switching legs 2 and 4 in diagrams (c) and (d) in Fig. 1 gives us the crossed Compton-like diagrams:

$$\begin{aligned} -\,iM_{c2} \equiv{}& (ig_e)^3\left(\frac{i}{q_2^2}\right) \\ &\times\left[\bar{u}_2\not{\epsilon}_1 i\frac{\not{p}_2-\not{p}_1+m}{(p_2-p_1)^2-m^2}\gamma^\mu u_0\right]\left[\bar{u}_4\gamma_\mu v_3\right], \end{aligned} \tag{7}$$

$$\begin{aligned} -\,iM_{d2} \equiv{}& (ig_e)^3\left(\frac{i}{q_2^2}\right) \\ &\times\left[\bar{u}_2\gamma^\mu i\frac{\not{p}_1+\not{p}_0+m}{(p_1+p_0)^2-m^2}\not{\epsilon}_1 u_0\right]\left[\bar{u}_4\gamma_\mu v_3\right]. \end{aligned} \tag{8}$$

2.1.3. Total matrix element for triplet photoproduction

By including the matrix elements shown in Fig. 1 and those given by exchanging lines 2 and 4, the full matrix element for the triplet photoproduction is calculable. The total matrix element M_{tot} is simply the sum of the eight matrix elements provided in Eqs. (1)–(8) above:

$$\begin{aligned} M_{\mathrm{tot}} ={}& M_a + M_b + M_c + M_d + \\ & M_{a2} + M_{b2} + M_{c2} + M_{d2}. \end{aligned} \tag{9}$$

2.1.4. Screening correction

The atomic electron on which the triplet photoproduction process takes place is embedded in a target material of atomic nuclei and other electrons; in this document, this material is referred to as the converter. The effects of the presence of these additional particles on the triplet production process are embodied in a screening function $S(q)$ (sometimes called an incoherent scattering function), as discussed in Refs. [2,3]. The correction due to the screening function $S(q)$ for triplet production on hydrogen is related to the atomic form factor $F(q)$ such that

$$S(q) = 1 - F^2(q), \tag{10}$$

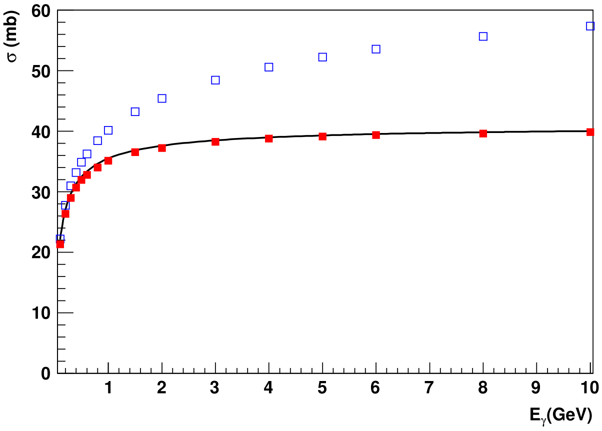

Fig. 2. (Color online) The total cross section for triplet photoproduction for beryllium as a function of incident photon energy. The red filled (blue open) squares represent generator results with (without) screening factor $S(q)$. The solid black line represents the NIST values [4].

where $F(q) = \left(1 + a^2q^2/4\right)^{-2}$, q is the momentum transfer to (i.e., the recoil momentum of) the atomic electron, and a is the Bohr radius [2].

The ratio of the triplet production cross section to the pair production cross section on an atom within the converter scales as the atomic number Z^{-1}. As a practical matter, then, the specific material chosen should have a low Z in order that this ratio is more favorable to triplet production. For the triplet detector described in this document, a beryllium converter foil was used, which has the lowest Z for a non-reactive metal ($Z = 4$). Thus, a beryllium screening function [3] was used for evaluation of the triplet photoproduction cross section below.

2.1.5. *Evaluation of the cross section*

The cross section can be evaluated using Monte Carlo simulation with event generator based on Eq. (9). We proceed in the following fashion. The events are generated randomly within the phase space of the reaction. For each event, the matrix element $|M_{\text{tot}}|^2$ is constructed from Eq. (9), averaged over initial spins and summed over final spins to obtain $\left\langle |M_{\text{tot}}|^2 \right\rangle$. For the case where the incident photon is polarized, the spin state of the photon is fixed in value while averaging over the initial spin states of the target electron. The cross section is obtained using

$$\frac{d\sigma}{d\Omega} = \frac{(2\pi)^2}{4km} \left\langle |M_{\text{tot}}|^2 \right\rangle \rho_f S(q), \tag{11}$$

where k is the incident photon energy and ρ_f represents the final-state phase space. Each event is then assigned a weight equal to the calculated cross section.

The calculated total cross section as a function of incident photon energy using Eq. (11) with and without consideration of the screening correction $S(q)$ is shown in Fig. 2.

2.1.6. *Comparison with experimental results*

The results from Eq. (11) are compared to the National Institute of Standards and Technology (NIST) cross sections for beryllium [4] in Fig. 2. In that figure, the solid black line represents the value of the total cross section given by NIST, and the results from the event generator are shown as squares; the results without the screening function $S(q)$ are shown as blue open squares, while red filled squares denote the results where that screening function has been included. As seen in the figure, the agreement between the event generator and NIST is excellent when the screening function is included. The agreement seen in Fig. 2 indicates that the triplet photoproduction process has been properly described by Eqs. (1)–(10) above.

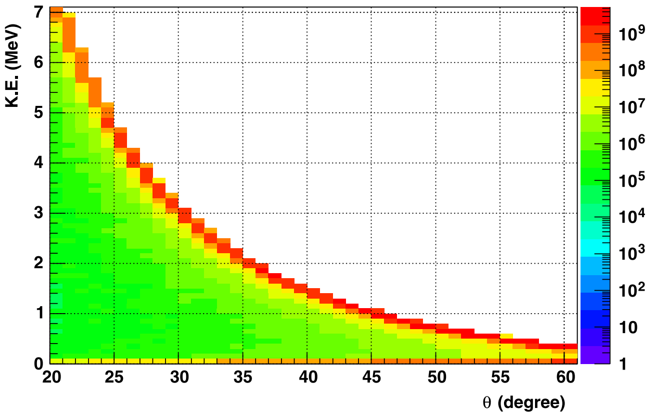

Fig. 3. (Color online) Cross-section-weighted kinetic energy versus polar angle for the recoil electron.

3. Design of a triplet polarimeter for Hall D

We describe in this section the design strategy for the triplet polarimeter TPOL, which detects the recoil electrons from the triplet process in order to measure the beam polarization of an intense (10^7–10^8 photons/s in the coherent peak) linearly-polarized photon beam with photon energies up to 9 GeV. The GlueX experiment [5] uses the linearly-polarized photon beam available in the newly-constructed Hall D at the Thomas Jefferson National Accelerator Facility (Jefferson Lab). GlueX will explore the properties of hybrid mesons, in which the gluonic field contributes directly to the quantum numbers of the mesons [6]. These explorations demand precise knowledge of the incident photon beam polarization.

The central component in a triplet polarimeter is the charged particle detector used for intercepting the recoil electrons from the photoproduction process. When considering the geometry of potential detectors for the recoil electron, the expected angular distribution and kinetic energies of the those electrons must be investigated. In Fig. 3, the cross-section-weighted kinetic energy versus polar angle θ for the recoil electron is plotted for incident photons with energies between 8 and 9 GeV. As seen in the figure, the polar angle increases as the recoil electron kinetic energy decreases. Thus, simply by inspection of Fig. 3 and considering the minimum kinetic energy for a recoil electron emerging from the production target, the maximum polar angle for a possible detector system can be estimated. For example, if the minimum desired kinetic energy for the recoil electron is 1 MeV, then the maximum polar angle of the detector should be about $\theta = 45°$.

With this initial design parameter established, the general dimensions of the detector geometry then can be investigated by simulation, using the same QED-based approach outlined in the previous section to generate events arising from the triplet photoproduction process. For purposes of simulation, events were generated with an idealized incident photon beam, where photons were polarized 100% in the x-direction with beam energies between 8 and 9 GeV. With this ideal beam, a histogram with 36 bins in azimuthal angle was created and filled with cross-section-weighted events.

Fig. 4 shows the cross-section-weighted counts versus azimuthal angle ϕ for recoil electrons with polar angle $\theta = 30°$. Since the polarization is set to $P = 1$ in these simulations, the resulting azimuthal distribution was fit to the functional form $A[1 - \Sigma\cos(2\phi)]$, where A and Σ were the fit parameters. Shown in Fig. 5 is the beam asymmetry (parameter Σ from the fit) as a function of polar angle θ. The asymmetry is largest when the recoil electron has polar angles near 0°and near 90°, but at large scattering angles the kinetic energy is very small, and at small angles one confronts the difficulty of placing a charged particle detector within a couple degrees of the beamline without moving that detector far away from the reaction vertex (and thereby greatly increasing the

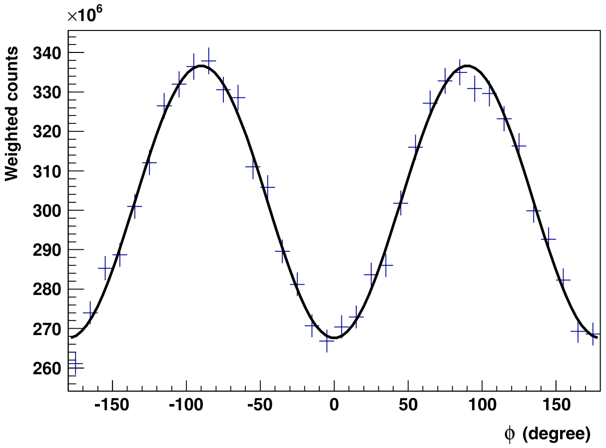

Fig. 4. Cross-section-weighted simulated triplet photoproduction events versus azimuthal angle ϕ for recoil electrons with polar angle $\theta = 30°$. Also shown by the solid curve is a fit to the azimuthal distribution using $A[1 - \Sigma\cos(2\phi)]$, with A and Σ as fit parameters.

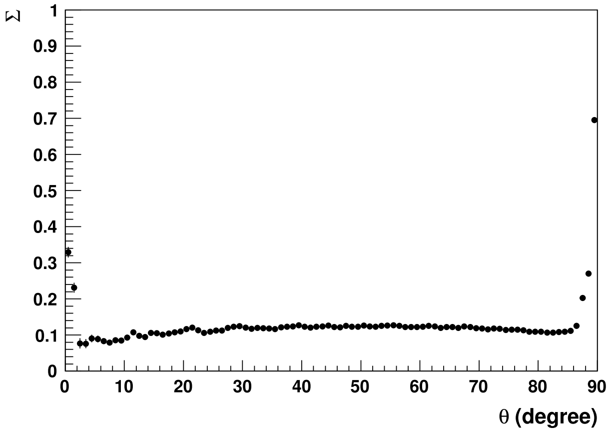

Fig. 5. Simulated beam asymmetry Σ as a function of polar angle, with no restrictions on the kinetic energy of the recoil electron.

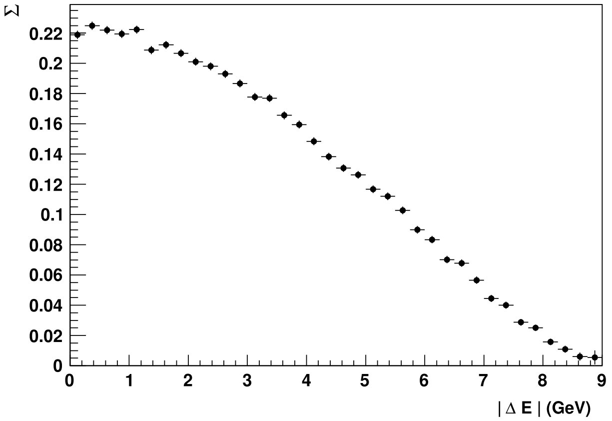

Fig. 6. Dependence of the beam asymmetry Σ on $|\Delta E|$, the difference between the kinetic energies of the produced e^+ and e^-.

size of the detection system). However, Fig. 5 indicates a relatively flat behavior at most intermediate polar angles, which in turn indicates a relative insensitivity to small deviations in the recoil electron polar angle when determining the beam asymmetry. When combined with the initial choice of the maximum polar angle from Fig. 3, the behavior seen in Fig. 5 provides a reasonable method for determining the minimum and maximum polar angles for the recoil electron detector, and, thus, the dimensions of that detector.

The beam asymmetry for triplet photoproduction also depends on the kinematics of the produced $e^+ e^-$ pair. Thus, a spectrometer is needed to determine the energies and trajectories for the produced electron and positron in order to fully specify the kinematics for the reaction. In Hall D, such a “pair spectrometer” [7] is located within the Hall D experimental area, and the converter is placed approximately 7.5 m upstream of the focal plane of that device. [Note that the location of the converter has changed since the publication of Ref. [7]).]

The Monte Carlo simulation can be used to explore the dependence of Σ on the energy difference ΔE between the kinetic energies of each member of the produced $e^+ e^-$ pair. As was seen in Fig. 3, the kinetic energy of the recoil electron is on the order of a few MeV for polar angles above 20°. This means that, for large recoil polar angles, nearly all the multi-GeV incident photon energy is divided between the members of the produced $e^+ e^-$ pair.

The simulated dependence of the beam asymmetry on the absolute value $|\Delta E| = |E_+ - E_-|$, where E_+ is the energy of the positron and E_- is the energy of the produced electron, is shown in Fig. 6. As the energies of the produced leptons become more equal (i.e., as $|\Delta E|$ becomes closer to 0), the beam asymmetry increases to a maximum of about 0.22. If a cut is applied such that events above a particular value of $|\Delta E|$ are removed, however, there necessarily will be a corresponding decrease in statistical accuracy in the measurement of that asymmetry. A particular choice for a $|\Delta E|$ cut must be considered in terms of its impact on the expected statistical uncertainty in the measured beam asymmetry.

The expected statistical uncertainty in the derived photon beam polarization is

$$\frac{\sigma_P}{P} = \frac{1}{\sqrt{N}}\sqrt{\frac{2}{\Sigma^2 P^2} - 1}, \tag{12}$$

where P is the polarization, σ_P the standard deviation in that quantity, N the number of triplet events surviving cuts, and Σ the beam asymmetry. For small values of ΣP.

$$\sigma_P \approx \frac{\sqrt{2}}{\Sigma\sqrt{N}}. \tag{13}$$

Thus, if we define a figure of merit (FOM) with the expression $\text{FOM} = 1/\sqrt{\Sigma^2 N}$, then FOM is directly proportional to the expected uncertainty in ΣP, with smaller values of FOM being more desirable. To relate the FOM to the derived value of Σ from the event generator, we create a “relative figure of merit” FOM_r such that $\text{FOM}_r = 1/\sqrt{\Sigma^2 N_w}$, where N_w is the number of cross-section-weighted events from the event generator. Fig. 7 shows FOM_r as a function of cut values in $|\Delta E|$, with the best FOM_r occurring when a cut is applied at about 6 GeV (events with $|\Delta E|$ greater than 6 GeV being removed from the analysis).

As a final design consideration, it is important to note that the observed recoil electron asymmetry will be altered if the recoil electron detector and the incident photon beam are not precisely coaxial. In practice, in our case, actual beam offsets should be rather small (typically less than a few hundred μm at Jefferson Lab) due to the care taken both in aligning the detector with the beamline and in delivering the incoming electron beam to the diamond radiator. Nonetheless, the effect of an offset in the photon beam spot position transverse to the recoil electron detector center must be explored. We simulated the detector response for different values of photon beam offset using unpolarized generated events. For that purpose, an unpolarized photon beam spot uniformly distributed over a 5 mm disk was simulated. Twenty evenly-spaced beam offsets ranging from 0.1 mm to 2.0 mm were analyzed. Fig. 8 shows a plot of cross-section-weighted events in blue for events generated with a 1-mm beam offset in the x-direction. Additionally, the figure shows a solid black line that represents a fit to the data, where the fit function is given by $A[1 + F_0\cos(\phi)]$, with A and F_0 being fit parameters. As seen from the figure, the function fits the result well,

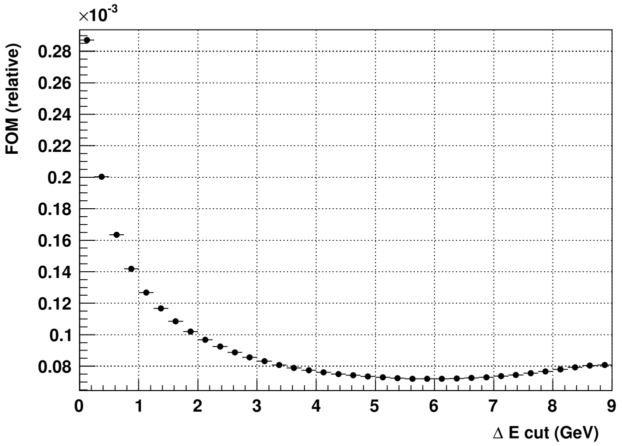

Fig. 7. Relative FOM as a function of the cut in energy difference $|\Delta E|$ (i.e., where energy differences greater than the $|\Delta E|$ value shown on the x-axis are neglected in the determination of relative FOM given on the y-axis). For each plot, the generated incident photon energy was uniformly distributed between 8 and 9 GeV.

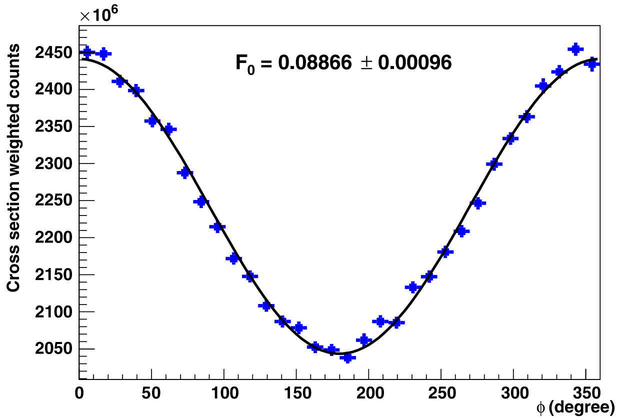

Fig. 8. The blue points are unpolarized Monte Carlo data with the incident photon-beam offset from the detector center by 1.0 mm in the x-direction. The solid line is a fit of the data with the function $A[1+F_0\cos(\phi)]$, where A and F_0 are parameters of the fit. The value of F_0 is shown on the plot and has a value of 0.089(1).

and in this case, produces a value of $F_0 = 0.089(1)$. In a similar manner, values of F_0 were determined for each of the generated beam offsets. The dependence of F_0 on the amount of generated beam offset was found to be remarkably linear, as seen in Fig. 9. The beam offset causes the observed azimuthal distribution to exhibit first-order Fourier moments; due to orthogonality, the beam offset has only a small impact on the extraction of the second cosine moment used to determine the beam asymmetry.

4. TPOL construction

Based on the design considerations outlined in the previous section, we have constructed a system for detection of recoil electrons following triplet photoproduction. The various elements of TPOL and details of construction are discussed in this section. The system consists of (1) a converter tray and positioning assembly, which holds and positions a beryllium foil converter within which the triplet photoproduction takes place; (2) a silicon strip detector (SSD) to detect the recoil electron from triplet photoproduction, providing energy and azimuthal angle information for that particle; (3) a vacuum housing containing the production target and SSD, providing a vacuum environment minimizing multiple Coulomb scattering between target and SSD; and (4) the preamplifier and signal filtering electronics within a Faraday-cage housing.

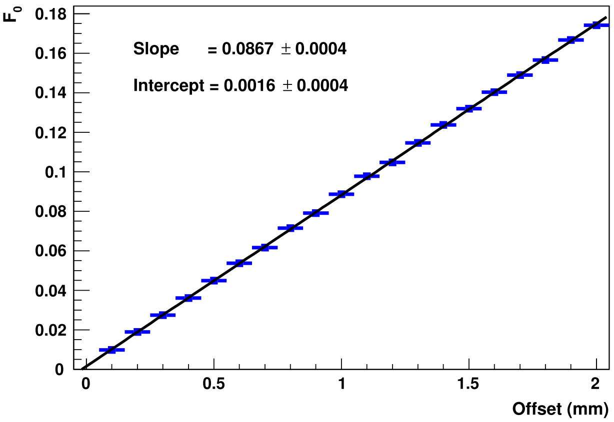

Fig. 9. Plot of the fit parameter F_0 in 8 versus beam offset in mm. The blue points are from fit results, and the solid line is a first degree polynomial fit to the data, where the slope and intercept are displayed on the figure.

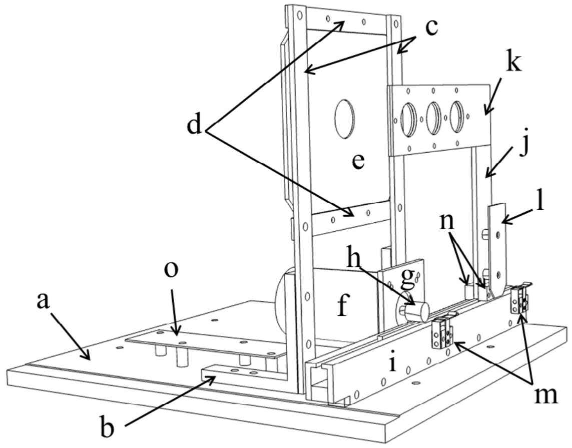

Fig. 10. The removable detector plate assembly (fasteners and wires not shown), shown in the orientation used for assembly and bench testing of the SSD and converter positioning system. During normal operation, the entire assembly shown here is inverted and inserted into the vacuum chamber, as seen in Fig. 12. The individual components include the mounting plate (a), leg support brackets (b), detector-frame legs (c), detector crossbars (d), silicon strip detector (e), stepper motor (f), mounting bracket (g), 0.5 module gear (h), rail guide (i), converter tray (j), converter tray cover (k), strike plate (l), limit switches (m), guide blocks (n) and wire-guide plate (o).

4.1. SSD mount, converter tray positioning system, and detector plate

As shown in Fig. 10, several components of TPOL are mounted on a 10 × 10 in^2 removable detector plate (labeled "a" in the figure), fabricated from 0.375-in-thick aluminum. The detector plate permits those components to be mounted, serviced, and tested together outside the vacuum chamber (described below) as needed, and then to be installed within the vacuum chamber for normal operation. The figure shows the detector plate in the orientation used for servicing and bench testing; during normal operation, the plate (along with the detector and converter tray assemblies) is inverted and slid onto mounting rails within the vacuum chamber, as discussed below.

The SSD (described below) is mounted on a rigid mounting frame, as seen in Fig. 10. Firmly attached to the detector plate ("a"), the SSD mounting frame consists of two leg support brackets ("b") to which are attached a pair of detector frame legs ("c"). A pair of detector cross bars ("d") are attached at right angles to the detector frame legs, and the SSD printed circuit mounting board ("e") is affixed to the detector cross bars. All pieces of the mounting frame are made of aluminum.

The polarimeter is installed within the collimator cave in the Hall D photon beam line during normal operation, which is a high radiation zone when the photon beam is incident on the device. An ability to remotely place and position converters of various thicknesses into the incident photon beam (or to remove them altogether) while maintaining the detector system under vacuum is desirable. This capability is provided by a converter positioning system shown in Fig. 10 (items “f” through “n”). A positioning stepper motor (“f”; described more fully below) is attached to the detector plate (“a”) by a mounting bracket (“g”) fixed to the plate. The positioning motor has a metric 0.5 module gear (“h”; gear teeth are not represented in the figure) that adjusts the position of a 0.5 module metal rail assembly contained within a rail guide (“i”). The rail assembly consists of the metal rail itself, sandwiched between two 0.125-in-thick aluminum pieces filed such that the rail assembly moves smoothly inside the rail guide. The converter tray (“j”) is a single, L-shaped piece of aluminum, with one leg attached to the rail and the other leg containing holes for up to three different converter foils. A removable cover (“k”) allows the converter foils to be installed and held in place on the converter tray.

The converter tray is moved by the stepper motor so as to position the converter of choice in the photon beam, with the motor operated remotely by the motor controller electronics. The stepper motor (Phytron VSS 43.200.1.2-UHVG [8]) is a two-phase stepper motor with 200 steps per revolution. The motor selected for this purpose can withstand a radiation dose of 1 MGy, and can operate at pressures as low as 7.5 nTorr. To ensure that the positioning system does not move the converter tray beyond acceptable bounds, a strike plate (“l”) attached to the converter tray through nylon spacers will engage one of two limit switches (“m”) if the converter tray moves beyond the preset range of motion. These normally-closed vacuum-rated limit switches (allectra 363-SWITCH-01) can operate with currents up to 1 A and provide, when engaged, an indication to the motor controller. Two guide blocks (“n”) fixed to the converter tray limit unwanted motion about the axis defined by the rail. While no fasteners or wires are shown in the figure, wires from the limit switches and from the motor are guided underneath a wire guide plate (“o”) attached to the detector plate using steel spacers; the wire guide plate keeps wires in place when the detector plate is inverted and placed within the vacuum housing.

4.2. Silicon strip detector

The recoil electrons from triplet photoproduction are detected by an S3 double-sided silicon strip detector manufactured by Micron Semiconductor [9]. The detector provides energy and trajectory information for those particles. The S3 has 32 azimuthal sectors on the ohmic side and 24 concentric rings on the junction side. The detector has an outer active diameter of 70 mm and an inner active diameter of 22 mm. The thickness of the silicon is 1034 μm, and the material is fully depleted with a bias potential of 165 V. During normal operation, the SSD is operated at the manufacturer’s suggested operating voltage of 200 V.

4.3. Vacuum chamber

To minimize energy loss and multiple Coulomb scattering of the recoil electrons as they travel between the converter foil and the SSD, the detector plate and all components shown in Fig. 10 are placed within a vacuum chamber manufactured by the Kurt J. Lesker Company [10]. (As noted above, the entire assembly shown in Fig. 10 is inverted before installing in the vacuum chamber.) The vacuum chamber, with interior volume 12 × 12 × 12 in^3, is physically located in the Hall D collimator cave just upstream of the pair spectrometer. Using the manufacturer’s web application, the design of one of their standard steel box chambers was modified to include ports and flanges for the purposes described below. Support brackets for positioning the detector plate and hardware shown in Fig. 10 were welded to the interior upper horizontal surface of the chamber by the manufacturer. The vacuum chamber walls themselves are made of 0.5-in-thick 304 stainless steel.

(a) Front view of vacuum chamber.

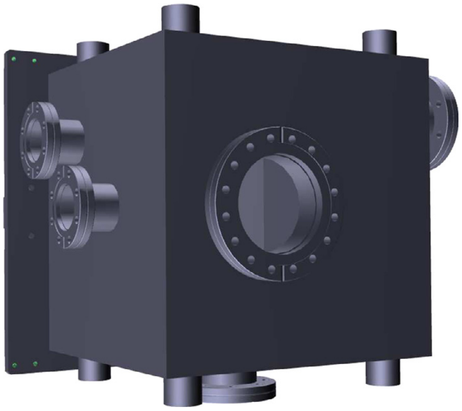

(b) Rear view of vacuum chamber.

Fig. 11. Vacuum chamber housing TPOL components. In (a), the photon beam enters from the right, while in (b) the photon beam enters from the left. The functions of the various ports and flanges are discussed in the text.

The exterior of the vacuum chamber is illustrated by the drawings provided in Fig. 11. On the downstream side of the chamber (seen at left in Fig. 11a) are three vacuum conflat flanges. The uppermost 4.5-in-diameter flange is used for routing cables related to the converter tray positioning system (items “f” through “n” in Fig. 10) described above. The lower flange (rotatable, 3.375-in-diameter) provides connection to the beam pipe, and the remaining flange (3.375 in diameter) is used to connect an auxiliary vacuum pump. An access door shown in Fig. 11a, constructed from a 1-in-thick 6061-T6 aluminum plate, includes a viewport (3.25×5.25 in^2) with a borosilicate glass cover. The back of the chamber seen in Fig. 11b has a 6-in-diameter flange for routing signal cables from the SSD. A flange located on the bottom of the chamber (4.5 in diameter) is used for mounting a turbomolecular vacuum pump. Two 3.375-in-diameter flanges are located on the upstream side (left side of Fig. 11b) of the vacuum chamber; the uppermost flange is for an auxiliary vacuum gauge, while the other (rotatable) flange is used as the port for the photon beam entrance, and is coupled to the photon beamline.

An interior view of the vacuum chamber is provided in Fig. 12. The SSD, attached to a (yellow) printed circuit board, is shown attached to the SSD mounting frame described above. As seen in the figure, handles of 304 tubular stainless steel (Grainger 4LAF8) are installed on the detector plate to assist removal and insertion. Fig. 12 also shows Kapton-insulated wires (30 AWG, Accu-Glass Products 112739) running from the far side of the SSD printed circuit board to a 6-in-diameter electrical vacuum feedthrough flange. The feedthrough flange contains two 50-pin connectors (Accu-Glass Products 50D2-600). The SSD-facing ends

Fig. 12. (Color online) Interior view of vacuum chamber, with detachable plate, converter tray positioning system and silicon strip detector installed. See Fig. 10 for details of the detector plate assembly.

of each Kapton wire are mated to the SSD printed circuit board using a standard wire-to-board connector (Yamaichi NFS64A0111), while the ends facing the feedthrough flange are crimped to female, gold-plated sockets (Accu-Glass Products 111652), which have then been inserted into a commercially-available 50-socket glass-filled dyiathilate high-vacuum D-connector (Accu-Glass Products 110007). One of the D-sub connectors routes signals for the SSD azimuthal sectors, while the other D-sub passes the signal lines for the concentric rings.

4.4. Detector electronics

As noted above, signals from the SSD are passed from the vacuum chamber through an electrical vacuum feedthrough flange containing two 50-pin D-sub connectors. The face of the feedthrough flange that is at atmospheric pressure is housed in a metal box enclosure serving as a Faraday cage for the preamplifier electronics. Signals from the downstream (azimuthal sector) side of the SSD are fed through the vacuum flange into a charge-sensitive preamplifier manufactured by Swan Research [11]. (At present, wires from the concentric ring side are connected to ground; a future upgrade will provide preamplifier electronics for the rings.)

The photograph in Fig. 13 shows an interior view of the preamplifier enclosure attached to the back of the vacuum chamber. The ring side cables run from the D-sub to ground through a terminal block (black rectangular box attached to the preamp enclosure floor), while the sector side cables (RG-178 braided coaxial) run from the D-sub to SMA connectors on the preamplifiers, which are housed in two metal boxes.

To reduce exterior electromagnetic signal interference, the box is lined with a layer of copper foil. While not easily seen in the figure, the stands used to attach the preamp boxes to the enclosure also are lined with copper foil on the side facing the preamp boxes, with that foil making good contact with the preamp boxes and the foil lining of the enclosure. The copper foil is attached to ground at several points through wires leading to a terminal block mounted to bottom wall of the enclosure. Attached to the left and right outside walls of the enclosure are two 80-mm case fans (Enermax UC-8EB) to provide cooling. On the interior side of the holes required for the fans, copper mesh (16 strands per inch with 0.011 inch diameter strands) are installed for additional electromagnetic shielding.

Each preamplifier box requires a positive and negative 12 V potential. In Fig. 13, SMA cables with end caps marked black are negative 12 V preamp supplies. Red markings are above the SMA connectors that supply positive 12 V. The SMA cable on the top preamplifier box passes the bias voltage to the sector side of the SSD.

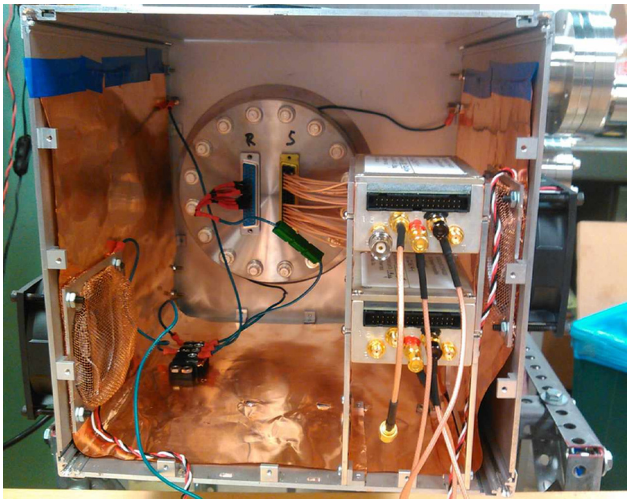

Fig. 13. (Color online) Interior view of preamplifier enclosure, with the front panel removed. Two sets of preamplifiers are housed in the two metal boxes mounted on standoffs at right in the foreground. Thin copper foil is used to line the top, bottom, and side walls of the enclosure.

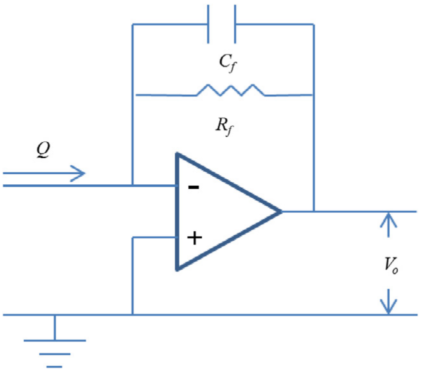

Fig. 14. Simplified circuit diagram of the charge-sensitive preamplifier used to process signals from the silicon strip detector in TPOL. The feedback capacitance (C_f) and resistance (R_f) determine the signal fall time presented at V_0.

In the depletion region of the silicon detector, an electron–hole pair is created for each 3.6 eV of energy deposited. The electrons are collected on the positive side of the potential (sector side of the detector), while the holes are swept towards the ring side (ground). These signals are fed to charge-sensitive preamplifiers manufactured by Swan Research (BOX16CHIDC/CHARGE8V). A simplified circuit diagram for the charge-sensitive preamplifier is given in Fig. 14. The feedback capacitance (C_f) and resistance (R_f) determine the signal fall time. For TPOL, $C_f = 0.2$ pF and $R_f = 30$ MΩ were chosen, resulting in a fall time of 6 μs. The rise time for the signal is determined by the charge collection time of the detector and by the response time of the preamplifier. Optimal sensitivity S_o of the preamplifier is obtained by a feedback capacitance such that $S_o = 1/C_f$, which leads to $S_o \approx 250$ mV/MeV.

Electronic filters and amplifiers were added to the output of the charge-sensitive preamplifiers in order to reduce unwanted noise and to provide a small amount of signal shaping before passing the signals to analog-to-digital converters within the GlueX electronics.

4.5. TPOL installation

The assembled TPOL is shown in Fig. 15 installed within the collimator cave in the Hall D beamline, appearing as three boxes attached to one another. The largest box at the rear is the vacuum chamber, while

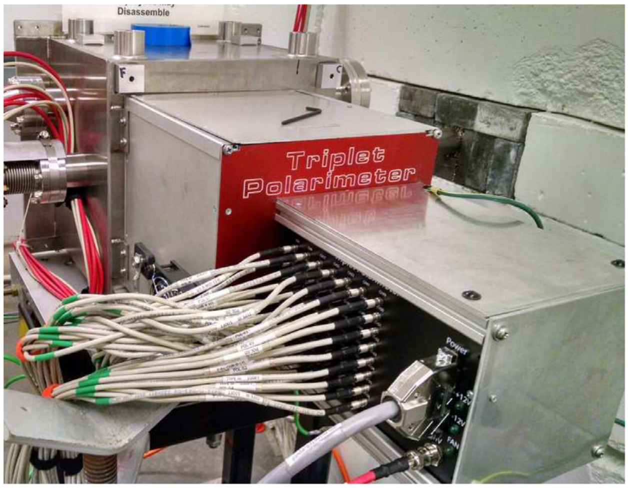

Fig. 15. (Color online) Triplet polarimeter installed in the Hall D beamline. The photon beam transits from left to right in this photograph within the beam pipe seen at rear left. The largest box at rear/left is the TPOL vacuum chamber.

the middle box is the preamplifier enclosure. The smallest box (closest to the viewer) is a signal distribution box that routes voltages and signals to and from the preamplifiers. The cables attached to the distribution box are the signal lines (white), high voltage bias (red) and low voltage (gray).

In operation, the TPOL vacuum box is coupled directly to the evacuated beamline through which the polarized photon beam passes. A diamond serves as the coherent bremsstrahlung photon production target for the Hall D photon beam, and is located upstream of the TPOL detector. Upon entering TPOL, the photon beam passes into whichever beryllium converter is positioned in the beam. Triplet photoproduction takes place within the converter material, with the recoil electron being detected by the SSD within the TPOL vacuum chamber. Produced electron–positron pairs, as well as any photons that did not interact with the converter material, pass through the downstream port of the vacuum box into the evacuated beamline, which in turn passes through a shielding wall (seen at right in the photograph) into the Hall D experimental area. The e^+e^- pair then enters the vacuum box and magnetic field of the GlueX pair spectrometer, while photons continue through an evacuated beamline to the target region of the GlueX detector. During normal running conditions, the photon beamline and TPOL vacuum chamber are operated at approximately 10 μTorr.

5. Analyzing power for TPOL

5.1. Analyzing power Σ_A for a given E_γ bin

Based on the layout of the Hall D beamline, the design of the Hall D pair spectrometer, and the physical location and geometry of the TPOL components provided in Section 4, the accuracy of beam polarization measurements performed by TPOL can be estimated. The triplet production beam asymmetry Σ discussed in Section 2 includes only the effects of triplet photoproduction. In real materials, recoil electrons passing through the converter material produce δ-rays, which also will be seen in the charged particle detector. Further, δ-rays also will be produced by the leptons from pair production in the converter material. Rather than the triplet beam asymmetry Σ, then, what is measured in practice by TPOL is the analyzing power Σ_A, which includes effects both from triplet production and from δ-rays. The actual azimuthal variation in yield Y measured experimentally, then, is

$$Y = A[1 - B\cos(2\phi)] = A[1 - P\Sigma_A\cos(2\phi)], \tag{14}$$

where P is the photon beam polarization. Hence, the photon beam polarization is $P = B/\Sigma_A$, and P can be derived if the analyzing power Σ_A is determined. This analyzing power will vary based on the photon beam energy E_γ.

Simulations for evaluating the analyzing power Σ_A for TPOL for a single energy bin with E_γ = 8–9 GeV are described here as an example. To make such an evaluation, the components and geometry as constructed and installed were coded into a GEANT4 simulation of TPOL along with a realistic intensity profile of the incident photon beam determined by QED calculations of coherent bremsstrahlung. The event generator described in Section 2 was used to model the triplet photoproduction within the beryllium converter material. The photon beam strikes the TPOL converter approximately normal to and centered on the converter foil. The nominal centerline and direction of the photon beamline determines the z-axis of the simulation coordinate system. To model production from the photon beam within the converter foil, the production vertices for triplet photoproduction events were distributed uniformly in the z-direction throughout the converter thickness, while the transverse profile of the vertex distribution used a realistic beam spot collimated within a diameter of 5 mm. A 76.2-μm-thick beryllium converter was simulated. Generated events were passed through the GEANT4 detector simulation.

In order to model the actual energy resolution of the detector and associated electronics, the recoil electron energy deposition for each azimuthal sector of the SSD was randomly reassigned by way of a normal distribution centered at the observed energy with a standard deviation of 30 keV (the choice of standard deviation is explained later in this document). Within any given simulated TPOL event, a TPOL hit was defined as a hit where a single azimuthal sector was struck by a recoil electron with energy deposition greater than 160 keV. Once the number of TPOL hits was established for a simulated event, only those events with a single TPOL hit having an energy deposition greater than 230 keV were further processed.

In the simulation, events were required to have an associated pair energy compatible with the energy acceptance of the Hall D pair spectrometer (PS). For an event to be considered as valid in this simulation, the energy difference of the pair $|\Delta(E)|$, defined as in Section 3, had to satisfy the following inequalities:

$$|\Delta(E)| < \Delta(E_{\max 1}) \tag{15}$$

and

$$|\Delta(E)| < \Delta(E_{\max 2}), \tag{16}$$

where

$$\Delta(E_{\max 1}) \equiv +1.0(E_{e^+} + E_{e^-}) - 6.6\ \text{GeV} \tag{17}$$

$$\Delta(E_{\max 2}) \equiv -1.0(E_{e^+} + E_{e^-}) + 13.6\ \text{GeV}. \tag{18}$$

In Hall D of Jefferson Lab, the pair spectrometer was constructed such that the accepted ΔE region as a function of incident photon energy lay within the red diamond region shown in Fig. 16. (For future running periods of GlueX, the pair spectrometer will be set such that the maximum acceptance will be near 9 GeV.)

To obtain the azimuthal yield distribution resulting from all these processes, the Monte Carlo events passing the criteria described above had the azimuthal sector hits binned in incident photon energy and azimuthal angle, with each event weighted by the cross section. In order to determine the analyzing power Σ_A, the photon beam polarization was set to unity (i.e., 100% linear polarization) solely to minimize the variance of Σ_A found from the simulation. For each photon energy bin, the azimuthal yield distribution was fit to the function $A_{t\delta}[1 - B_{t\delta}\cos(2\phi)]$, where $B_{t\delta}$ represents the beam asymmetry observed for both triplet events and δ-ray contributions. To determine the analyzing power Σ_A, the effects of δ-rays coming from the leptons resulting from the pair production process also were included in the simulation. The

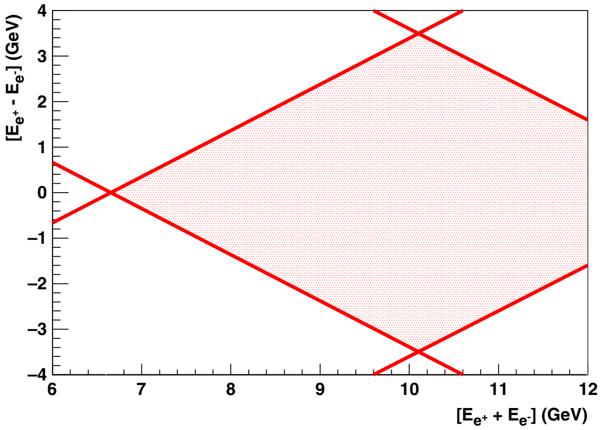

Fig. 16. (Color online) Plot of the difference $|\Delta E| = |E_+ - E_-|$, where E_+ is the energy of the pair-production-produced positron and E_- is the energy of the produced electron, versus the sum $|E_+ + E_-|$. The region between the red lines represents the fiducial region of the Hall D pair spectrometer for the Spring 2016 running of GlueX.

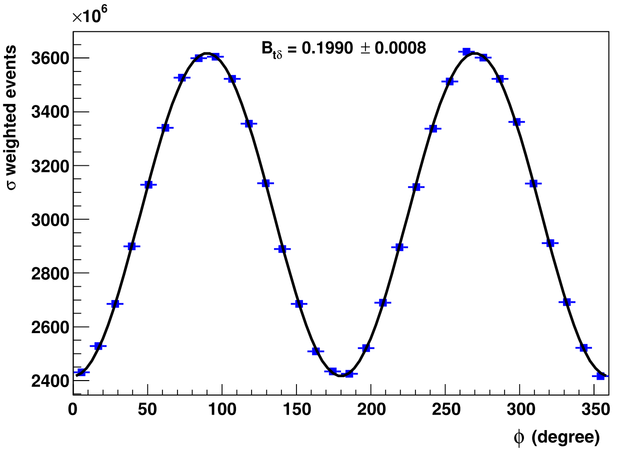

Fig. 17. Analyzing power extraction. The blue points are cross-section-weighted Monte-Carlo data for triplet events with incident photon beam energies between 8.5 and 8.6 GeV, including events arising from δ–rays. The black line represents a fit of the data to $A_{t\delta}[1 + B_{t\delta}\cos(2\phi)]$, where $A_{t\delta}$ and $B_{t\delta}$ are parameters of the fit. For this energy, the value of $B_{t\delta}$ found has a value of $B_{t\delta} = 0.1990(8)$.

pair-induced δ-ray contribution to Σ_A was included by treating that effect as a dilution. Essentially, including δ-rays from the pair production process, the equation for the yield Y is

$$Y = A_{t\delta}[1 - B_{t\delta}\cos(2\phi)] + A_{p\delta}, \tag{19}$$

where the yield from the pair-produced δ-rays is given as $A_{p\delta}$. As noted above in Eq. (14), this expression also may be written as

$$Y = A[1 - P\Sigma_A\cos(2\phi)], \tag{20}$$

where, setting $P = 1$ for these simulations,

$$\begin{aligned} A &\equiv A_{t\delta} + A_{p\delta}, \\ \Sigma_A &= B_{t\delta}\frac{A_{t\delta}}{A}. \end{aligned} \tag{21}$$

From the above equations, the analyzing power Σ_A is seen to be the $B_{t\delta}$ asymmetry diluted by a factor of $A_{t\delta}/A$. Therefore, a dilution factor was defined as $d = A_{t\delta}/A$, leading to the result that the analyzing power may be written as $\Sigma_A = B_{t\delta}d$.

The value of $A_{p\delta}$ was found by allowing only the created pairs from the generated triplet events to be processed through the detector simulation. The integrated detector response, weighted by the triplet cross section and passing all the analysis cuts, was then scaled by the ratio $R_{pt} = \sigma_p/\sigma_t$, where σ_p (σ_t) is the pair (triplet) production cross section given by NIST [4]. For beryllium, R_{pt} is found to vary quite slowly with energy, from $R_{pt} = 3.38$ at 8 GeV to $R_{pt} = 3.37$ at 10 GeV.

The yield distribution found from the simulations is shown in Fig. 17. When fit by the expression $Y = A_{t\delta}[1 - B_{t\delta}\cos(2\phi)]$, $B_{t\delta}$ was found to be 0.1990 ± 0.0008. The dilution factor determined from simulation was $d = 0.9575$, yielding an analyzing power $\Sigma_A = 0.1905(7)$.

In practice, the same procedure is used to determine the analyzing power Σ_A for a specific photon energy bin E_γ. The experimentally measured value of $B(E_\gamma)$ for that photon energy bin will indicate a photon beam polarization P given by $P(E_\gamma) = B(E_\gamma)/\Sigma_A(E_\gamma)$, as stated in Eq. (14).

The primary factors related to the determination of the analyzing power Σ_A now have been described. While much smaller in impact, an additional refinement is added to the analyzing power estimation by including the PS geometric acceptance. The PS has, in addition to the energy-dependent acceptance discussed above, a geometric acceptance for the lepton pairs attributable to the finite height (3 cm) of the individual PS detector elements. This geometric acceptance is also influenced by the nominal distance from the converter foil to the PS detector elements, taken to be 7.5 m. The simulation of these acceptance corrections included a realistic beam spot, the nominal distance the created pair travels before striking a PS detector, and the PS detector height. When these PS geometric considerations were included, the analyzing power increased by a factor of 1.0026 for the case where the incident photon was parallel to the floor (PARA); for the case where the incident photon was perpendicular to the laboratory floor (PERP), the asymmetry increased by a factor of 1.0057. These correction factors must be applied in the final determination of the beam polarization.

5.2. Rate dependence of the polarization determination

After all cuts have been applied, the detector accepts approximately 2% of the total triplet cross section. The design goal for the GlueX photon beam is to have a polarization of 0.4 and rate of 10^8 photons per second within the coherent peak energy range of 8.4–9.0 GeV. Given such a beam incident on a 75 μm thick beryllium converter, the expected TPOL rate surviving all cuts is 75 Hz (and perhaps as high as 10 kHz without cuts for the full incident photon-energy range), leading to an approximate statistical uncertainty in the TPOL determination of polarization of 0.014, after a single hour of production running.

5.3. Effects from variations in beam spot location

Systematic uncertainties associated with the uncertainty in beam spot location were estimated using simulations. Within the simulations, the realistic beam spot was collimated to have a diameter of 5.0 mm (same as the GlueX Spring 2016 runs) and was allowed to be displaced relative to the collimator center in steps of 0.1 mm from the nominal position over a grid with eleven bins in the horizontal (x_B) and vertical (y_B) directions. In addition to the beam center displacement relative to the collimator center, the collimator was varied in vertical displacement relative to the TPOL center. The horizontal (vertical) coordinate of the collimator relative to the TPOL center is called x_0 (y_0). The values of vertical displacement studied were $y_0 = 0.0, 0.1, 0.2, 0.3, 0.4, 0.5$ mm. In all cases the horizontal displacement of the collimator relative to the TPOL center was fixed to $x_0 = 0.0$.

The number of beam spot positions generated relative to the collimator center was 121 and the number of collimator positions relative to the TPOL center was 6. Thus, the total number of beam spot/collimator positions studied was 726. From the set of 726 combinations of beam spot and collimator positions, the value of F_0 was found. We take as a conservative estimate of possible beam/collimator positions those cases where $F_0 < 0.0225$. The requirement that $F_0 < 0.0225$ reduced the set of

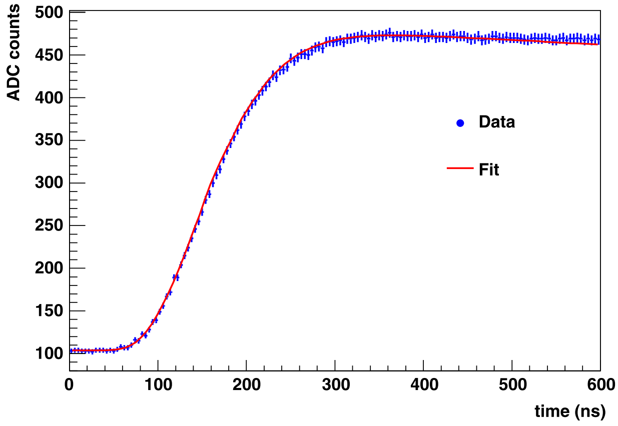

Fig. 18. (Color online) TPOL SSD signal ADC counts versus time for a typical event. The blue points are the data, while the red solid line represents the fit of the data to the SPICE waveform. (The error bars shown on the signal ADC counts are not meaningful and should be ignored.)

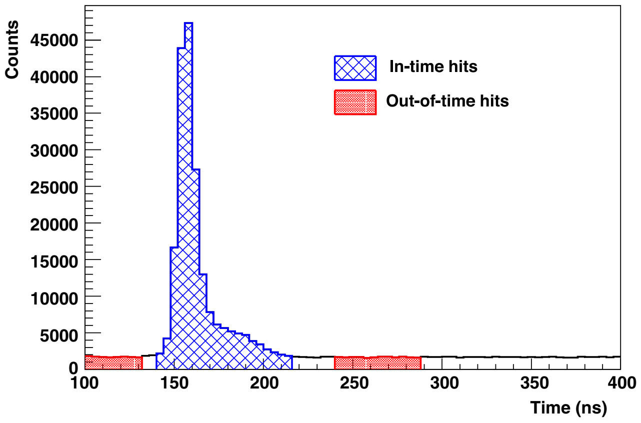

Fig. 19. (Color online) TPOL time relative to the PS trigger. The blue (cross-hatch) region represents events that are considered as being in time. The red (shaded) regions are where out-of-time events are defined.

726 combinations of beam spot and collimator positions to 30 cases that were further analyzed. From the 30 cases of beam/collimator positions compatible with the restriction that $F_0 < 0.0225$, the largest deviation from the ideal case (100% polarized beam with collimator and beam centered on TPOL) was found to be 0.71%.

6. Analysis of spring 2016 data

Comparisons of the simulations described above with the actual performance of this device have been made using data obtained in Hall D at Jefferson Lab in Spring 2016. Those comparisons are presented here to illustrate that the device is well-understood and performing as expected.

As was discussed in Section 4.4, an electron–hole pair is created for each 3.6 eV of energy that was deposited in the silicon strip detector (SSD). During the Spring 2016 running, this electronic signal from the SSD was amplified and filtered using the electronics described above, and the resulting signal was then passed to a flash ADC. The flash ADC used for the TPOL in the Spring 2016 running had 4096 channels distributed uniformly over a 2-volt range with a 250 MHz sampling rate.

For the first priority dataset from Spring 2016, the ADC threshold for the amplified and filtered SSD signal was set to 133 ADC counts. The TPOL ADC information was read out whenever a signal above threshold was in coincidence with a GlueX or pair spectrometer (PS) trigger. PS-triggered events were skimmed from the full dataset for further analysis. The PS skim included relevant PS, TPOL, and tagger information, and all the variables required for further analysis were placed into a ROOT tree.

A SPICE-generated waveform simulation of the signals emerging from the TPOL electronics was created by using the LTspice IV program (electronic circuit simulator) [12], with a custom representation of the preamp, filter and amplifier electronics. The input signal for the LTspice program was a 10 μA pulse over a 5-ns duration (3.12×10^5 electrons), corresponding to about 1.12 MeV of energy deposition when assuming an electron–hole pair for each 3.6 eV.

Within an event, every sector with a maximum ADC value greater than the readout threshold (133 ADC counts) was fit to the SPICE-generated waveform plus a constant (representing the baseline). The magnitude, time of the signal, and baseline constant were the only variables allowed to vary. A typical fit of the data to the SPICE waveform is shown in Fig. 18, where the actual data are shown as blue points and the resulting SPICE waveform fit is represented as a solid red line. As seen in the figure, the shape of the SPICE waveform represents the data well.

To calibrate the simulated energy deposition in the device, the energy determined by the SPICE fit was taken as an initial estimate. The peak energy was then matched to the value given by the Monte Carlo using a single multiplicative constant for each sector. The initial energy given by the SPICE fit was generally found to be very close to the final value, with the calibration constant for any given sector only differing from unity by about 10%.

For the time information in the simulation, the point along the fitted waveform halfway between the minimum and maximum signal voltage was taken to correspond to the time of the signal. Fig. 19 shows the timing of the TPOL events, where the blue region defined the TPOL in-time events and the red regions the TPOL out-of-time events. From the events given in Fig. 19, the ratio of signal to background was found to be 5.1.

Most electrons striking the SSD are minimum ionizing, and these particles transit the entire depth of the SSD, leaving electron–hole pairs throughout the thickness of the detector. However, the lowest-energy recoil electrons penetrate and stop very close to the upstream surface of the SSD. These low-energy electrons thus deposit all their energy close to the upstream side of the SSD. As a result, the signal formation (the accumulation of the charge represented in the generated electrons and holes) for such a low-energy recoil electron is delayed when compared to the minimum-ionizing case. This delay in the signal formation causes the tail seen in the timing distribution shown in the blue region of Fig. 19, ranging from about 170 to 210 ns.

The tagger time spectrum is shown in Fig. 20. For the tagger, the in-time events are defined as being within ±2 ns and the out-of-time events are defined as being the two beam-buckets that have tagger time between −14 and −6 ns.

To determine the energy resolution of the triplet polarimeter, a plot of energy deposition from data was compared to energy deposition from Monte Carlo where the simulated results had differing resolutions applied. The manner in which the detector resolution was expressed in the simulation was by smearing the Monte Carlo energy deposition using a normal distribution. For each generated event, the value of energy deposition found from the simulated detector response was replaced by a random value arising from a normal distribution that had a center coinciding with the original energy deposition and a fixed standard deviation. The standard deviation of the normal distribution then corresponded to the detector/electronics resolution of the TPOL.

Variations of the location of the deposition of energy within the SSD can result in different charge collection efficiencies and timing. Values for estimates of TPOL energy resolution were explored in a Monte Carlo study of energy deposition. Of the resolution values explored, some are shown in Fig. 21, with the standard deviation of the smeared energy shown on the plot. As can be seen in Fig. 21, smearing the energy

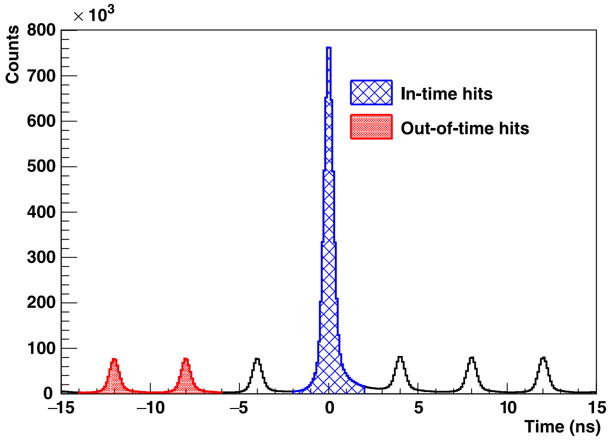

Fig. 20. (Color online) Tagger time relative to the PS trigger. The blue (cross-hatch) region represents events that are considered as being in time. The red (shaded) regions are where out-of-time events are defined.

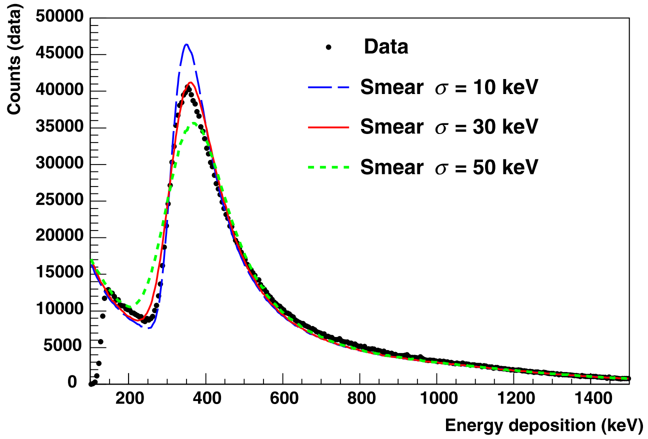

Fig. 21. (Color online) Energy deposition. Blue represents data. Blue long-dashed line is Monte Carlo with smear parameter set to 10 keV. Red solid line is Monte Carlo with smear parameter set to 30 keV. Green short-dashed line is Monte Carlo with smear parameter set to 50 keV.

deposition using a value for the standard deviation equal to 30 keV appeared to reproduce the data fairly well. The simulation was refined by using a double Gaussian function to represent a correction to shift the data to better align with the simulation results. The double Gaussian "shift function" is shown in Fig. 22 and gives the potential shift in energy deposition versus the value of energy deposition seen in the data. Using the double Gaussian given in Fig. 22, a comparison of Monte Carlo to shifted real data is seen in Fig. 23. As shown in Fig. 23, this comparison of the shifted data to the simulation results works quite well. This smearing function suggests that the energy calibration likely is accurate to within 80 keV. The possible systematics associated with this uncertainty in the energy calibration and energy resolution will be discussed below.

For a further comparison, actual TPOL data from the Spring 2016 running that passed the same cuts applied to the simulation (described in Section 5) were placed in a histogram with out-of-time hits subtracted. Due to limited statistics in the Spring 2016 run, when the incident photon energy was less than 8.4 GeV or greater than 9.4 GeV, the tagger information was neglected. Thus, only the tagged-photon flux within the energy range from 8.4 to 9.4 GeV is analyzed in the following comparisons. The events coming from the red shaded region seen in Fig. 19 represented the TPOL out-of-time hits, and these were subtracted from those events with TPOL in-time events coming from the blue cross-hatched region.

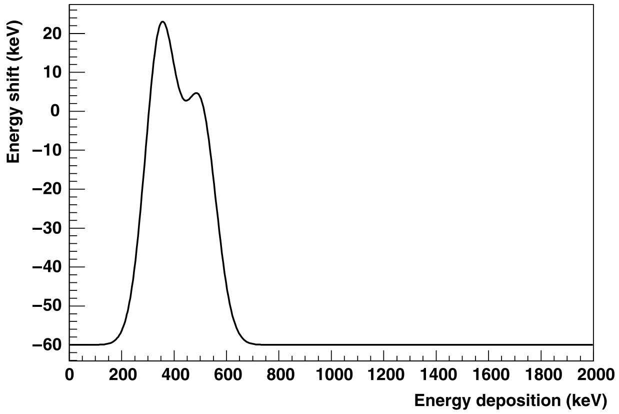

Fig. 22. Potential energy shift versus energy deposition. The black line represents the shifted distribution described in the text.

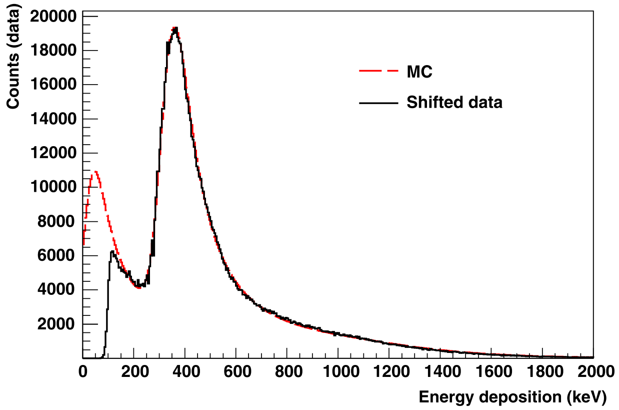

Fig. 23. (Color online) Comparison of Energy deposition simulation to data when data has been shifted. The black solid line represents data that has been shifted in energy by an amount shown in Fig. 22. The red dashed line is Monte Carlo with smear parameter set to 30 keV.

When the incident photon energy was within the range 8.4–9.4 GeV, a two-stage out-of-time subtraction was performed. In the first stage, each TPOL event coming from either blue (TPOL in-time) or red (TPOL out-of-time) region from Fig. 19, had tagger out-of-time hits subtracted, where the tagger in-time hits are defined as having tagger time relative to PS within ±2 ns (see Fig. 20) and tagger out-of-time hits are defined as being between −14 and −64 ns (two beam buckets). The tagger out-of-time hits were weighted by a factor of 1/2 to account for the fact that two beam buckets were used for the tagger out-of-time subtraction. The second stage of the subtraction was to simply subtract the TPOL out-of-time hits from the TPOL in-time events.

The photon beam polarization orientation for a particular run is defined as being either PARA or PERP in orientation. The PARA orientation had the photon beam polarization orientation parallel to the laboratory floor, while the PERP orientation had the photon beam polarization plane perpendicular to the floor. An example of an out-of-time subtracted yield distribution for PARA and PERP with incident photon energies at 8.95 GeV is provided in Fig. 24, where the solid line is a fit to the data using the function $A[1 \pm B\cos(2\phi - 2\phi_0)]\epsilon(\phi)$, where the $+$sign is for the PERP setting, while the $-$ sign is for PARA. The acceptance function $\epsilon(\phi)$ is due to the beam offset described in Section 3, and has the form $[1 + F_0\cos(\phi - \phi_1)]$. For the PARA setting, $F_0 = 0.011(1)$, which roughly corresponds to a beam offset of 0.1 mm. For the case of PERP, the first moment was found to be even closer to zero ($F_0 = 0.005(2)$).

The determination of the degree of photon beam polarization was found by taking the value of B and dividing that value by the corresponding value of the analyzing power Σ_A obtained from the simulation

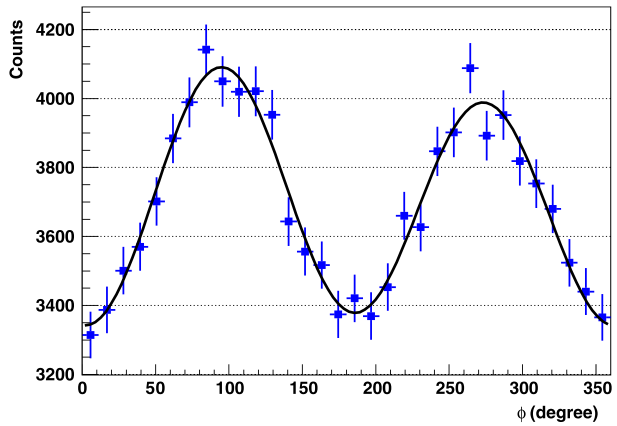

(a) PARA setting.

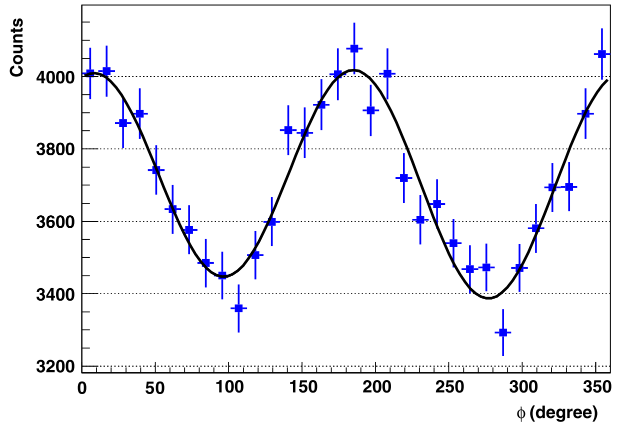

(b) PERP setting.

Fig. 24. Counts versus azimuthal angle for TPOL events with $E_\gamma = 8.95$ GeV. In (a), the results for the PARA setting are shown, while in (b) the PERP setting is given.

(described in Section 5). A plot showing the polarization for PARA and PERP orientations as a function of incident photon energy is given in Fig. 25, where the blue points are for PARA and the red points are for the PERP orientation.

7. Systematic uncertainties in the photon beam polarization estimate

Uncertainties in the analyzing power Σ_A determined in the previous section yield a corresponding systematic uncertainty in the beam polarization P made with TPOL. The possible sources and estimated contributions of uncertainty in the analyzing power are described in this section.

7.1. Converter thickness

As discussed above, the passage of the recoil electrons and the e^+e^- pair through the converter material results in the generation of δ-rays which strike the SSD. The δ-rays are treated as a dilution of the measured beam asymmetry, as given in Eq. (21). Uncertainties in estimating the dilution factor contributes a corresponding systematic uncertainty to the beam asymmetry measurement. The number of δ-rays produced and the amount of recoil electron rescattering that occurs within the converter material both depend upon the thickness of the converter, which directly impacts the value of analyzing power. An uncertainty in the number of δ-rays generated arises from any uncertainty in the thickness of the converter material.

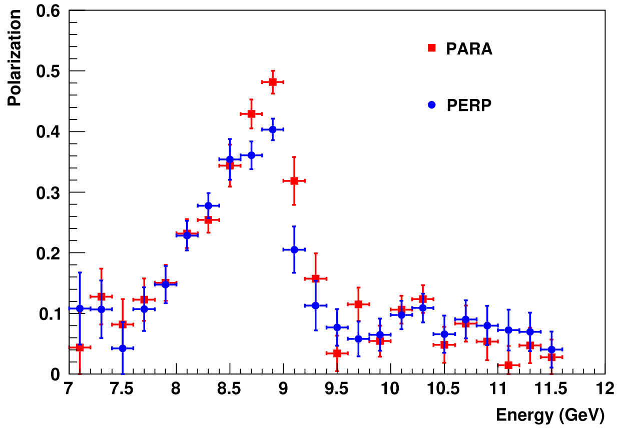

Fig. 25. (Color online) Polarization versus E_γ. Red squares represent results from the PARA setting, while blue circles represents PERP results.

The manufacturer of the beryllium converter gives a tolerance of 5×10^{-4} inch (12.7 μm) for the stated thickness of the material. Assuming this tolerance represents an amount equivalent to three standard deviations of thickness variation over the photon-illuminated converter, then the standard deviation for this thickness measurement (and the corresponding variation in the geometry within TPOL) would be equivalent to an uncertainty of 4.2 μm. To explore the uncertainty resulting from this much variation, the analyzing power was determined for converter thicknesses of 72.0, 76.2 (nominal) and 80.4 μm. The largest percent difference in analyzing power was found from the case using the nominal converter thickness and that for the 80.4 μm converter thickness. Based on this percentage difference, the estimated systematic uncertainty in the analyzing power Σ associated with the converter thickness was determined to be $\sigma_{\Sigma_A}/\Sigma_A = 0.53\%$.

7.2. SSD energy threshold and calibration

The energy calibration for each sector of the SSD is determined based on the observed pulse height distribution and the estimated energy deposited in that sector. An energy threshold is required for each particle detected in order for that interaction to be classified as a detector hit, and the value of that energy threshold is based on the energy calibration. The energy cut used in the analysis of data and simulation results was 230 keV. Uncertainties in the energy calibration and the energy resolution of the device affect the accuracy with which the analyzing power is determined.

The uncertainty in the beam asymmetry coming from the uncertainty in the location of the cut on energy deposited in the SSD was determined in the following fashion. In initial tests, the observed energy deposition spectra for all sectors of the SSD were found to be within 80 keV of the Monte Carlo simulations of those spectra (see Figs. 22 and 23), over an energy deposition range from 0.1 to 3 MeV. The analyzing power derived with a cut on the energy deposition at 190 keV is 99.1% of the value that would have resulted had the cut been placed at 270 keV (that is, a difference of 80 keV in the energy cut). Therefore, the systematic uncertainty contribution to the analyzing power due to uncertainties in the position of the energy cut was taken to be $\sigma_{\Sigma_A}/\Sigma_A = 0.9\%$.

Based on initial tests, the energy resolution has been observed to have a standard deviation of about 30 keV. Taking extreme cases, where the resolution is, at best 10 keV, and at worst 50 keV (see Fig. 21), the systematic uncertainty associated with energy resolution can be estimated by simulation. The analyzing power using a 10 keV smear was found to be 0.5% larger than with a 50 keV smear. Thus, a conservative estimate for the systematic uncertainty of the analyzing power due to the energy resolution is taken to be $\sigma_{\Sigma_A}/\Sigma_A = 0.5\%$.

Table 1
Estimated systematic uncertainty in the TPOL determination of beam asymmetry Σ_A.

Source of uncertainty	Estimated uncertainty ($\sigma_{\Sigma_A}/\Sigma_A$)
Converter thickness	0.53%
Threshold, resolution, and calibration	1.0%
Converter-to-detector distance	0.54%
Beam offset	0.71%
Simulation statistical precision	0.2%
Estimated total uncertainty in Σ_A	1.5%

Initial tests found that the sector-by-sector energy calibration was consistent within a standard deviation of 3 keV. A total of 12 trials were simulated where the energy cut for a sector came from a random normal distribution of standard deviation equal to 3 keV. Using this procedure, the uncertainty in the analyzing power due to the sector-by-sector calibration was found to be 0.1%.

Combining all these SSD energy threshold and energy calibration uncertainties results in an uncertainty of 1.0% due to those effects.

7.3. Detector-to-converter distance

The distance from the converter foil to the TPOL detector determines the minimum and maximum polar angle that the recoil and δ-rays make with the detector. Any uncertainty in the distance from the converter foil to TPOL detector will impact the value of analyzing power. However, because the SSD is very sensitive, the detector surface cannot be physically touched by survey equipment once it is positioned in the vacuum chamber. Instead, the survey determines the distance from the center of the foil to the downstream face of the PCB that holds the SSD; that distance was found to be 34.9 mm. Since the PCB is 2.4 mm thick, the distance from the foil to the center of the PCB is 33.7 mm, and that estimated distance was used in simulations of an uncertainty in detector-to-converter distance. The SSD is 1 mm thick, and its exact placement in the beam direction within the PCB was taken to be uncertain to ±0.7 mm. Simulations of the analyzing power for an SSD displaced +0.7 mm and −0.7 mm from the nominal position in the direction of the incident photon beam indicated that the analyzing power uncertainty due to this position uncertainty is 0.54% .

7.4. Photon beam offset

As described above (Section 3), any transverse offset of the photon beam axis from the nominal center of the TPOL SSD will affect the value extracted for the analyzing power. Uncertainties in that position (or offset) thus result in an additional uncertainty in the beam asymmetry extracted. As discussed in Section 3 the systematic uncertainty associated with the beam offset is 0.71%.

7.5. Simulation statistical precision

The finite number of events simulated leads to a statistical limitation as to how well the analyzing power can be determined from the number of simulated events processed during the simulation. For example, the uncertainty in analyzing power due to simulation statistics over the range 8.4–9.0 GeV (the energy range used in [13]) was found to be $\sigma_{\Sigma_A}/\Sigma_A = 0.2\%$. That value can be taken as the systematic uncertainty in the analyzing power due to the simulation statistical precision.

7.6. Beam asymmetry uncertainty

The total estimated systematic uncertainty in the analyzing power $\sigma_{\Sigma_A}/\Sigma_A$ based on TPOL arising from all contributions discussed above is summarized in Table 1. Once each contribution is summed in quadrature, the total systematic uncertainty estimate in the beam asymmetry $\sigma_{\Sigma_A}/\Sigma_A$ is 1.5%.

7.7. Beam polarization uncertainty

In practice, as indicated by Eq. (14), the photon beam polarization is given by $P = B/\Sigma_A$. The uncertainty in the photon beam polarization σ_P is determined by combining the systematic uncertainty for the beam asymmetry Σ_A described above (summarized in Table 1 and denoted as σ_{Σ_A}) with the statistical uncertainty in the yield (B in Eq. (14)) measured during an experiment for the photon energy range of interest. In the absence of any other sources of uncertainty (for example, contributions attributable to radiative corrections to the beam asymmetry for the triplet photoproduction process, which are expected to be small relative to those uncertainties discussed above), then, the uncertainty σ_P in the photon beam polarization P will be

$$\frac{\sigma_P}{P} = \sqrt{\left(\frac{\sigma_{\Sigma_A}}{\Sigma_A}\right)^2 + \left(\frac{\sigma_B}{B}\right)^2}. \tag{22}$$

Acknowledgments

The authors gratefully acknowledge conversations and discussions with Leonard Maximon and with colleagues in the GlueX Collaboration. Work at Arizona State University was supported by the National Science Foundation under award PHY-1306737, and work at the University of Connecticut was supported by the National Science Foundation under award PHY-1508238. Jefferson Science Associates, LLC operated Thomas Jefferson National Accelerator Facility for the United States Department of Energy under US Department of Energy contract DE-AC05-06OR23177.

References

[1] K. Mork, Pair production by photons on electrons, Phys. Rev. 160 (1967) 1065–1071. http://dx.doi.org/10.1103/PhysRev.160.1065.

[2] L. Maximon, H. Gima, Pair production in the field of atomic electrons, Phys. Rev. A 23 (1981) 172–185. http://dx.doi.org/10.1103/PhysRevA.23.172.

[3] J. Hubbell, W. Veigele, E.A. Briggs, R. Brown, D. Cromer, R. Howerton, Detection of recoil electrons in triplet photoproduction, J. Phys. Chem. Ref. Data 4 (1975) 471–538. http://dx.doi.org/10.1063/1.555523.

[4] Experimental triplet and pair photoproduction cross sections were obtained using the web application XCOM available at http://physics.nist.gov/PhysRefData/Xcom/html/xcom1.html.

[5] (GlueX Collaboration), H. Al Ghoul, et al., First results from the GlueX experiment, in: Proceedings, 16th International Conference on Hadron Spectroscopy (Hadron 2015): Newport News, Virginia, USA, September 13–18, 2015, AIP Conf. Proc. 1735 (2016) 020001. http://dx.doi.org/10.1063/1.4949369. arXiv:1512.03699.

[6] C.A. Meyer, E.S. Swanson, Hybrid Mesons, Prog. Part. Nucl. Phys. 82 (2015) 21–58. http://dx.doi.org/10.1016/j.ppnp.2015.03.001. arXiv:1502.07276.

[7] F. Barbosa, C. Hutton, A. Sitnikov, A. Somov, S. Somov, I. Tolstukhin, Pair spectrometer hodoscope for Hall D at Jefferson Lab, Nuclear Instrum. Methods A 795 (2015) 376–380. http://dx.doi.org/10.1016/j.nima.2015.06.012.

[8] The stepper motor was purchased from Phytron GmbH, http://www.phytron-elektronik.de.

[9] A data sheet for the Micron Semiconductor S3 device is available at http://www.micronsemiconductor.co.uk/pdf/s.pdf.

[10] Kurt J. Lesker box vacuum chambers available for purchase are described at http://www.lesker.com/newweb/chambers/std_boxchamber.cfm.

[11] Information regarding the Swan Research preamplifiers is available at http://www.swanresearch.xorgate.com.

[12] The LTspice SPICE simulator software is available at http://www.linear.com/solutions/ltspice.

[13] (GlueX Collaboration), H. Al Ghoul, et al., Measurement of the beam asymmetry Σ for π^0 and η photoproduction on the proton at $E_\gamma = 9$ GeV, Phys. Rev. C 95 (2017) 042201. http://dx.doi.org/10.1103/PhysRevC.95.042201. arXiv:1701.08123, URL https://link.aps.org/doi/10.1103/PhysRevC.95.042201.